THE UNIVERSITY *of* EDINBURGH

Edinburgh Research Explorer

CFD modelling and simulation of drill cuttings transport efficiency in annular bends: Effect of particle sphericity

OPEN ACCESS

Accepted Manuscript

CFD modelling and simulation of drill cuttings transport efficiency in annular bends: Effect of particle sphericity

Emmanuel I. Epelle, Dimitrios I. Gerogiorgis
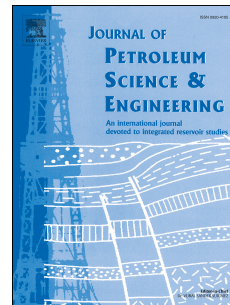
Please cite this article as: Epelle, E.I., Gerogiorgis, D.I., CFD modelling and simulation of drill cuttings transport efficiency in annular bends: Effect of particle sphericity, *Journal of Petroleum Science and Engineering* (2018), doi: 10.1016/j.petrol.2018.06.041.

(a) Severe particle deposition
d = 0.004 m, ψ = 0.50
CMC fluid
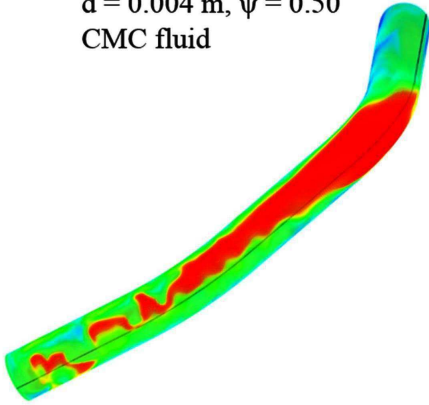
(b) Mild particle deposition
d = 0.004 m, ψ = 0.50
CMC + Bentonite fluid
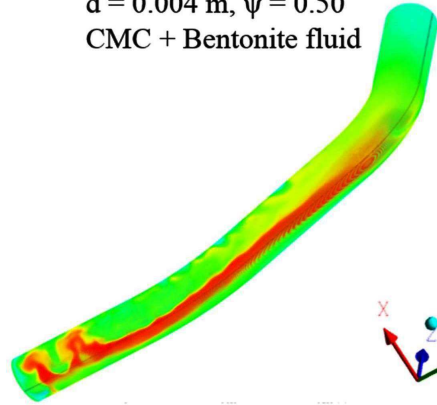
Particle volume fraction, φ

0.629
0.472
0.315
0.157
0.000

CFD Modelling and Simulation of Drill Cuttings Transport Efficiency in Annular Bends: Effect of Particle Sphericity

Emmanuel I. Epelle and Dimitrios I. Gerogiorgis*

Institute for Materials and Processes (IMP), School of Engineering, University of Edinburgh, The King's Buildings, Edinburgh, EH9 3FB, United Kingdom

*Corresponding author: D.Gerogiorgis@ed.ac.uk (+44 131 6517072)

Abstract

Accurate prediction of the flow behaviour of drill cuttings carried by a non-Newtonian fluid in an annular geometry is important for the successful and efficient design, operation, and optimisation of drilling operations. Although it is widely recognised that practical drilling operations hardly involve perfectly spherical cuttings, the relative ease in mathematical description coupled with speedy computation are the main reasons for the prevalence of this simplifying assumption. The possibilities offered by the modification of the interphase exchange coefficient of the Syamlal-O'Brien model as well as its scarce implementation in literature have motivated the authors to delve into this area of research as far as the transport phenomena of non-spherical drill cuttings is concerned. Another aspect of this work was influenced by the need to understand the flow dynamics around bends (horizontal to inclined and inclined to vertical sections) during deviated drilling operations using two high viscosity muds (0.5% CMC and 0.5% CMC + 4% Bentonite mud). The Eulerian-Eulerian model was adopted for this study while considering particle sphericities of 0.5, 0.75 and 1 and diameters of 0.002 m, 0.003 m, 0.004 m, 0.005 m and 0.008 m respectively. It was discovered that particle deposition intensifies at the inclined-to-vertical bend compared to other locations in the flow domain. We also observe increased dispersion effects and transport velocities of non-spherical particles compared to particles of a perfectly spherical geometry. Furthermore, an improvement in the rheological properties of the drilling mud shows a remarkable increase in cuttings transport efficiency especially with the smaller particles. However, increased deposition of larger particles still poses a challenge to the wellbore cleaning process despite this rheological enhancement. The proposed CFD modelling methodology is thus capable of providing critical insight into the dynamics of cuttings transport, and the resulting computational observations are consistent with relevant experimental investigations.

Keywords: Particle sphericity, drag coefficient, annular bends, volume fraction

Highlights

1. Shape of drill cuttings incorporated via the sphericity factor in the interphase momentum exchange coefficient of the Syamlal-O'Brien drag model affect the overall transport properties.
2. Upper bend (inclined-to-vertical) is the most susceptible location to cuttings deposition.
3. Increasing the mud viscosity does not always guarantee easy wellbore cleaning.
4. Sphericity influences the transport velocity of larger cuttings to a greater extent compared to smaller-sized cuttings.
5. The assumption of perfect sphericity could yield as high as 11% decrease in pressure drop relative to the actual pressure drop of the irregular particles considered.

1

1. Introduction

The current status of understanding of the motion of non-spherical particles during drilling operations has some limitations; one of which is related to the obvious simplicity perfectly spherical particles provide particularly in modelling. Particles encountered during drilling are hardly spherical; hence, extra parameters are necessary for increased accuracy as far as their flow description and prediction are concerned. Exact mathematical quantification of the geometry of complex irregular solid particles is difficult; however, the concepts of particle equivalent diameter and shape factors of different types (Corey shape factor, roundness and sphericity) are usually employed in several process engineering applications. Despite the existence of these descriptors of particle irregularity such as: Wadell roundness, Dobkins and Folk roundness, Power's roundness, Wadell sphericity, Krumberin sphericity, Sneed and folk sphericity and Riley sphericity[1], the Wadell sphericity is the most widely implemented single measure of particle shape characterisation. This is undoubtedly as a result of its ease of implementation with existing drag models for spherical particles.

Comer and Kleinstreuer[2] reported specifically that the assumption of a spherical shape could result in the underestimation of the drag coefficient by 30% for some spheroids. This discrepancy could widen when the particle's orientation with respect to the bulk fluid motion plays an important role due to irregularities in particle shape. Just as most research endeavours on the motion of solid particles in a fluid consider mainly spherical particles,[3,4,5,6] most investigations accounting for particle sphericity are concerned with Stokes flow at low particle Reynolds number.[7,8,9,10] Adjustments of the drag coefficient for higher Reynolds numbers significantly depend on empirical data and sometimes the particle orientation. The dominating and crucial role of the drag force in determining particle behaviour in a fluid is the rationale behind several modifications of the drag coefficient compared to other forces acting on a particle moving in a fluid.

It is also important to note that most of the studies in literature that account for the impact of particle shape on fluid-solid multiphase flows have been carried out for single-particle flow or multi-particle flow systems in fluidised bed applications; during which the carrier fluid is mostly a gas or a Newtonian fluid[1,11,12,13,14]. Very little attention has been paid to oil and gas drilling systems. However, the works of Akhshik et al.[15] Yilmaz[33], Al-Kayeim et al.[35], and Mohammadzadeh et al.[37] address to different extents the impact of sphericity using Finite Volume Analysis of the governing equations. Akhshik et al.[15] evaluated the fluid-particle flow patterns, particle velocity and concentration profiles for non-spherical particles using a coupled CFD/DEM model and discovered that particle sphericity plays a major role in fluid-solid interaction. Yilmaz[33] used the Discrete Phase Model (DPM) with the Rosin-Rammler size distribution to study the moving bed velocity of particles with a sphericity of 0.1. By using particles of three different sphericities and the Eulerian-Eulerian model, Al-Kayeim et al. [35] observed a slight improvement in cleaning performance as the sphericity increased. In the work of Mohammadzadeh et al.[37], the Particle Transport Ratio (PTR) was analysed as a function of the viscosfier content of a drilling fluid using spherical and non-spherical particles. Their implementation the EE model produced a significant influence of the sphericity on the PTR. Celigueta et al.[40] presented a novel FEM-DEM method for studying non-spherical cuttings transport in a non-Newtonian fluid with successful description of particle behaviour.

Our previous work[16] considered turbulence modulation by cuttings of different sizes during drilling operations but however, neglected flow complexities that arise due to the shape of the particles. It is expected that the particle shape will have substantial effects on the turbulent modulation and dispersion characteristics as well as the particle-fluid interactions. Considering this limitation, and the scarceness of published literature which address this challenge, we aim to incorporate the effect of particle shape into the modelling equations by a slight modification on the exchange coefficient in the Syamlal-O'Brien (SO) model. Furthermore, we analyse solid-liquid flow in a fairly different geometry compared to what has been previously applied using two types of drilling mud. Such geometry (Figure 1) considered here is often realisable in extended-reach and deviated well drilling. We aim not only to provide some insight into the dynamics of the transport process but also to present a modification strategy which could be extended for capturing more advanced phenomena such as turbulence.

2

2. Methodology

2.1 CFD model description

The Eulerian-Eulerian (EE) multiphase flow model describes the behaviour of multiple, separate and yet interacting phases.[17] Unlike the computationally expensive Lagrangian-Eulerian (LE) model in which statistically computed particle trajectories are evaluated for a large number of particles, the EE model evaluates the particle concentration across the entire flow field while considering the particle fluxes with significantly reduced computational cost. The occurrence of particles with non-uniform size and shape distribution (which is accounted for in the LE model) is almost inevitable in most industrial applications and this could be a limiting factor of the EE model, except additional transport equations (continuity and momentum balance equations) are incorporated and solved for each size and shape. The interaction between phases is handled by pressure and interphase mass and momentum exchange coefficients; these coefficients are key parameters of the EE model and determine the peculiarities of the flow[13]. Furthermore, their description and formulation principles depend on the type of phases present (solid, liquid or gas) i.e. fluid-fluid, solid-solid or fluid-solid exchange coefficients.

2.2 Drag Modification

It has been proven that the shape of a particle strongly influences the drag force experienced by the particle and its terminal velocity during flow; thus, improved flow prediction can be attained by better shape description of the particles[18]. Accounting for the particle sphericity is usually done in two ways: first, is the modification of the drag coefficient according to experimental findings i.e. for a specific shape, the drag coefficient can be found as a function of the Reynolds number in a similar way to the expressions for perfectly spherical particles. This is however cumbersome, considering the large range of possible shapes particles could take in practical operations. Second, is the use of size and shape factors to describe an equivalent spherical particle.[10] In a bid to implement the second method, we have modified the Syamlal-Obrien model by re-defining the exchange coefficient in the expression (Eq. 4). Several published works[12,13,18] reveal comparable performance between the Gidaspow model and the Syamlal-Obrien model; however, the relative ease of implementation of this slight modification (Eq. 11) in the exchange coefficient compared to that of Gidaspow influenced our choice of the SO drag model. Essentially, the need for a switch/blending function to ensure a smooth transition between conditions of high and low particle concentration is not necessary when using the SO model. This absence of the switch function in the SO model, makes the application of the shape modification factor relatively straight forward (Section 2.2).

2.3 Mathematical formulation

2.3.1 Continuity

The volume fraction of each phase is calculated from the continuity equation:

$$\frac{1}{\rho_{rs}}\left(\frac{\partial}{\partial t}(\alpha_s \rho_s) + \nabla \cdot (\alpha_s \rho_s \vec{v}_s) = \sum_{l=1}^{n}(\dot{m}_{ls} - \dot{m}_{sl})\right) \tag{1}$$

2.3.2 Fluid-Solid momentum equation

$$\frac{\partial}{\partial t}(\alpha_s \rho_s \vec{v}_s) + \nabla \cdot (\alpha_s \rho_s \vec{v}_s \vec{v}_s) \tag{2}$$

$$= -\alpha_s \nabla p - \nabla p_s + \nabla \cdot \bar{\bar{\tau}}_q + \alpha_s \rho_s \vec{g} + \sum_{l=1}^{N}(K_{ls}(\vec{v}_l - \vec{v}_s) + \dot{m}_{ls}\vec{v}_{ls} - \dot{m}_{sl}\vec{v}_{sl}) + (\vec{F}_s + \vec{F}_{lift,s}$$

$$+ \vec{F}_{vm,s} + \vec{F}_{td,s})$$

Where $\vec{v}_s$ is the velocity of the solid phase, $\vec{v}_l$ is the velocity of the liquid phase, α_s is the volume fraction of the solid phase, ρ_s is the density of the solid phase, ρ_l is the liquid phase density, $\dot{m}_{ls}$ and $\dot{m}_{sl}$ characterise the mass transfer between solid and liquid phases respectively, $\vec{v}_{ls}$ and $\vec{v}_{sl}$ are the interphase velocities, g is the

acceleration due to gravity, ρ_{rs} is the phase reference density, $\vec{F}_s$ is an external body force, $\vec{F}_{lift,s}$ is the lift force, $\vec{F}_{vm,s}$ is the virtual mass force and $\vec{F}_{td,s}$ is the turbulent dispersion force (applicable to turbulent flows only). The equation for the force terms are detailed in the Fluent theory manual.[17] Depending on the prevalent flow regime and transport phenomena, some terms (such as the turbulent dispersion force, $\vec{F}_{td,s}$ and mass transfer terms, $\dot{m}_{ls}$ and $\dot{m}_{sl}$) of the Eq. 2 become redundant. Thus, the equation becomes:

$$\frac{\partial}{\partial t}(\alpha_s \rho_s \vec{v}_s) + \nabla \cdot (\alpha_s \rho_s \vec{v}_s \vec{v}_s)$$

$$= -\alpha_s \nabla p - \nabla p_s + \nabla \cdot \bar{\bar{\tau}}_q + \alpha_s \rho_s \vec{g} + \sum_{l=1}^{N} (K_{ls}(\vec{v}_l - \vec{v}_s)) + (\vec{F}_s + \vec{F}_{lift,s} + \vec{F}_{vm,s})$$

(3)

2.3.3 Fluid-Solid exchange coefficient

In the SO model,[19] the fluid-solid exchange coefficient is defined as:

$$K_{sl} = \frac{3\alpha_s \alpha_l \rho_l}{4 v_{r,s}^2 d_s} C_D \left(\frac{Re_s}{v_{r,s}}\right) |\vec{v}_s - \vec{v}_l|$$

(4)

Several models exist for determining the fluid-solid interphase exchange coefficient: they include the Gidaspow, Di-Felice, Gibilaro, Syamlal-O'Brien, Wen-Yu, Ergun, Ma-Ahmadi, and others. However, the extent of application of these models depends majorly on the velocity of flow and the degree of granular phase packing.[1] The drag function (C_D) in Eq. 4 has a form derived by Dalla Valle,[20] Re_s is the particle Reynolds number,

$$C_D = \left(0.63 + \frac{4.8}{\sqrt{\frac{Re_s}{v_{r,s}}}}\right)^2$$

(5)

$$Re_s = \frac{\rho_l d_s |\vec{v}_s - \vec{v}_l|}{\mu_l}$$

(6)

$v_{r,s}$ is the terminal velocity correlation for the solid phase and μ_l the viscosity of the liquid phase.

$$v_{r,s} = 0.5 \left(A - 0.06 Re_s + \sqrt{(0.06 Re_s)^2 + 0.12 Re_s (2B - A) + A^2}\right)$$

(7)

Where

$$A = \alpha_l^{4.14}$$

(8)

and

$$B = 0.8 \alpha_l^{1.28} \ for \ \alpha_l \leq 0.85 \ and \ B = 0.8 \alpha_l^{2.65} \ for \ \alpha_l > 0.85$$

(9)

α_l is the liquid phase volume fraction.

2.3.4 Particle sphericity

Although the particle diameter appears also in the definition of the Reynolds Number, in the SO model (Eq. 6), the sphericity coefficient is implemented only in the equation describing the interphase momentum exchange coefficient. A similar modification strategy was adopted for the Gidaspow model in the work of Sobieski.[13] It is worth mentioning that the drag coefficient is only found in the Wen-Yu formula of the Gidaspow model[21]; this suggests that its significance is restricted to dilute granular flow (i.e. at low particle concentration, so that there is

free movement in the liquid phase). Conversely, the Ergun equation of the Gidaspow model is applied for dense particle flows. It can thus be inferred that a better modification strategy for the SO model, especially due to the prevalence of dense granular flow in our application, is to introduce the sphericity directly into the exchange coefficient rather than the drag coefficient. Additionally, several experimental measurements of drag coefficient for a wide range of particle shapes exist, but a functional relationship of this coefficient in terms of the Reynolds number, particle orientation and geometry is very scarce. This further substantiates our approach of incorporating the shape descriptor into the interphase exchange coefficients (Eq. 11).

$$\acute{K}_{sl} = \eta K_{sl} \tag{10}$$

Where

$$\acute{K}_{sl} = \frac{3\alpha_s \alpha_l \rho_l}{4 v_{r,s}^2 \psi d_s} C_D \left(\frac{Re_s}{v_{r,s}}\right) |\vec{v}_s - \vec{v}_l| \tag{11}$$

$$\eta = \frac{1}{\psi} \tag{12}$$

$$\psi = \frac{A_s}{A_c} \tag{13}$$

Where η is the drag modification factor, ψ is the particle sphericity (the ratio between the surface area of a sphere with the same volume as the particle - A_s, and the surface area of the actual particle - A_c), d_s is the volume equivalent diameter (diameter of a sphere having the same volume as the non-spherical particle). It is worth emphasizing that the sphericity coefficients are model constants selected during computations and no experiments have been performed to determine the values for rock cuttings. Experimental determination of cuttings transport phenomena which measure the sphericity of the rock cuttings are rare; this scarcity in data can be partly attributed to the difficulties of surface area measurement of irregular particles. It has been argued that the application of the sphericity coefficient is more suitable for particles whose sphericity coefficient approach unity[18] and that the accuracy of sphericity-based correlations reduces when complex shapes with high aspect ratios and very low sphericities are modelled[27]. However, recent improved applications of the DEM-CFD coupled technique have shown remarkable predictions of pressure drop in fluidised beds[38]. This recommendation and the continuous phase assumption of the discrete phase in the Eulerian-Eulerian (EE) model constitute the rationale for choosing particle sphericities shown in Table 1. The application of this model provides some fundamental insight into the modifications non-spherical particles add to the flow explained subsequently in the result section.

2.3.5 Closures

Not only the fundamental the mass and momentum balance equations are solved; mathematical descriptions (closure models) of specific flow properties and effects, such as the granular temperature and viscosity, solids and frictional pressure have to be accounted for.

2.3.5.1 Granular viscosity – Syamlal et al.[22]

$$\mu_s = \frac{\alpha_s d_s \rho_S \sqrt{\Theta_S \pi}}{6(3 - e_{SS})} \left[1 + \frac{2}{5} g_{0,SS} \alpha_S (1 + e_{SS})(3e_{SS} - 1)\right] \tag{14}$$

2.3.5.2 Granular bulk viscosity – Lun et al.[23]

$$\lambda_S = \frac{4}{3} \alpha_S^2 \rho_S d_S g_{0,SS} (1 + e_{SS}) \left[\frac{\Theta_S}{\pi}\right]^{1/2} \tag{15}$$

2.3.5.3 Frictional Viscosity – Schaeffer[24]

Asides gravity and drag force, frictional force between particles could significantly affect particle behaviour at high particle volume fractions.

$$\mu_{S,fr} = \frac{p_S \sin \phi}{2\sqrt{I_{2D}}} \tag{16}$$

Where p_S is the solids pressure, ϕ is the angle of internal friction and I_{2D} is the second invariant of the deviatoric stress tensor.

2.3.5.4 Frictional Pressure – Johnson and Jackson[25]

$$P_{friction} = Fr \frac{(\alpha_s - \alpha_{s,\min})^n}{(\alpha_{s,max} - \alpha_s)^p} \tag{17}$$

Where coefficient $Fr = 0.05$, $n = 2$ and $p = 5$

2.3.5.5 Solids Pressure – Lun et al.23

$$p_s = \alpha_s \rho_S \Theta_S + 2\rho_S(1 + e_{SS})\alpha_S^2 g_{0,SS}\Theta_S \tag{18}$$

Where e_{SS} is the coefficient of restitution for particle collisions; $g_{0,SS}$ is the radial distribution function and Θ_S is the granular temperature

2.3.5.6 Radial Distribution – Lun et al.[23]

$$g_{0,SS} = \left[1 - \left(\frac{\alpha_s}{\alpha_{s,max}}\right)^{\frac{1}{3}}\right]^{-1} \tag{19}$$

2.3.5.7 Granular temperature transport equation (algebraic formulation)

$$0 = (-p_S\bar{\bar{I}} + \bar{\bar{\tau}}_s):\nabla\vec{v}_s - \gamma_{\Theta_S} + \phi_{ls} \tag{20}$$

$(-p_S\bar{\bar{I}} + \bar{\bar{\tau}}_s):\nabla\vec{v}_s$ is the generation of energy by the solid stress tensor; γ_{Θ_S} is the collisional dissipation of energy and ϕ_{ls} is the energy exchange between the fluid and solid phases.

2.3.5.8 Collisional dissipation of energy – Lun et al.[23]

$$\gamma_{\Theta_S} = \frac{12(1 - e_{ss}^2)g_{0,SS}}{d_S\sqrt{\pi}}\rho_S\alpha_s^2\Theta_S^{3/2} \tag{21}$$

2.4 Modelling assumptions and boundary conditions

- Particles and the conveying medium (non-Newtonian fluid) are regarded continuous.
- No-slip condition between continuous phases and the walls (drillpipe and wellbore).
- Particles are represented by mono-sized non-spherical and spherical geometries; the shape factor is not included in the lift coefficient and non-spherical particle orientation is not considered.
- There is no change in shape or mass due to particle-particle interactions.
- Restitution coefficients determine the friction between particles and pipeline walls (a value of 0.9 is adopted).
- Annular walls are assumed to be smooth (no roughness factor is incorporated).
- A fluid velocity inlet (shown in Table 1) and atmospheric pressure outlet.

- Particle inlet velocity of 0.5 m.s^{-1} is adopted.

2.5 Simulation strategy

In order to determine how strongly the simulation model changes with a change in the interphase momentum exchange coefficient (a function of particle sphericity), RANS equations were numerically solved using the finite volume formulation. The Semi-Implicit Method for Pressure Linked Equations (SIMPLE) was adopted as the pressure-velocity coupling scheme. Spatial discretization of all equations was carried out using the Quadratic Upstream Interpolation for Convective Kinematics (QUICK) method. In order to avoid divergence of numerical solution and non-physical flow patterns, convergence of the unsteady particle-fluid calculations is confirmed by negligible values (10^{-4}) at each time step of the global mass and momentum imbalances in the computational domain. A time step of 5.10^{-4} was used for the transient simulations (second order implicit) which were run for a total period of 5 seconds in each test case. Convergence was attained in less than 10 iterations of each time step. The difference between the averaged flow properties at this time and successive time steps was negligible (statistically steady-state condition). Computations were carried out on the University's high performance computing facility (Eddie mark 3 – Scientific Linux 7 Operating System) with 32 cores (2.4GHz Intel®-Xenon® CPU processor) and 64GB of RAM.
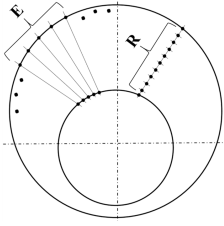
2.6 Fluid rheology, flow geometry and meshing

The properties of the drilling fluids (1 and 2) used in this study were adapted from the work of Abu-Jdayil and Ghannam[26]; their performances (transport efficiencies) were comparatively analysed using the power law (0.5% Carboxymethyl cellulose – CMC) and Herschel-Bulkley models (0.5% CMC + 4% Bentonite) for their rheological description. More simulation parameters are given in Table 1. A description of the flow geometry and the meshing style and associated properties is shown in Figure 1. A mesh independence study revealed that 665,600 elements were sufficient to obtain accurate results.

Table 1. Simulation input parameters

	Drilling Mud 1	**Drilling Mud 2**
Geometry		
Drill pipe diameter, d_{pipe} (m)	0.113	0.113
Wellbore diameter, d_{wb} (m)	0.180	0.180
Computational length, L (m)	2.340	2.340
Particle properties		
Cuttings diameter, d_s (m)	0.002, 0.003, 0.004, 0.005 and 0.008	0.002, 0.003, 0.004, 0.005 and 0.008
Cuttings density, ρ_s (kg.m^{-3})	2800	2800
Sphericity, ψ	0.50, 0.75, 1.00	0.50, 0.75, 1.00
Fluid properties		
Composition	0.5% CMC Solution	0.5% CMC + 4% Bentonite
Density, ρ_l (kg.m^{-3})	1000	1030
Yield stress, τ_0 (Pa)	0	46.5
Consistency index, K (Pa.s^n)	0.5239	0.6482
Flow behaviour index, n	0.60	0.7
Drilling variables		
Fluid circulation velocity, v_l (m.s^{-1})	0.8	0.8
Cuttings inlet velocity, v_s (m.s^{-1})	0.5	0.5
Drill pipe rotation, Ω (rpm)	100	100
Hole eccentricity, e	0.6	0.6

Table 2 shows the properties of the significantly different mesh resolutions tested. In the description of mesh divisions 'E by R', 'E' represents the number of edge division around the circular outer and inner sections of the annulus, and 'R' represents the radial face divisions of the circular section. Our choice of mesh used in this study was strongly influenced by the quality (Table 2) and the nature of results obtained as shown in Figure 2. We observe that upon successive refinements, the results produced by the finest resolution mesh ('70by30' – used as base case for pressure drop comparisons) differ insignificantly from the results of the '80by20' mesh, which we deem the most appropriate. It can also be observed in Table 2 that the average wall clock time for running a single simulation varies considerably with the mesh resolutions. By changing the resolution from '70by20' to '80by20', the run time is almost doubled; however, the higher skewness factor and lower orthogonality make this mesh ('70by20') less preferred.

Table 2. Mesh resolutions and properties

	Mesh Divisions	Total Faces (E×R)	No. of Nodes	No. of Elements	Min. ố	Max. ς	Max. AR	Min. Face Size	Max. Face Size	AWT (hr)
	50by10	500	143,550	130,000	0.36	0.79	9.01	0.0003	0.03	1.41
	60by20	1200	393,120	373,200	0.71	0.50	15.31	0.0003	0.03	3.60
	70by20	1400	536,550	509,600	0.47	0.70	13.03	0.0003	0.03	4.52
	80by20	**1600**	**700,560**	**665,600**	**0.72**	**0.49**	**11.42**	**0.0003**	**0.03**	**8.17**
	70by30	2100	792,050	764,400	0.42	0.70	19.61	0.0003	0.03	10.66

AWT – Average wall clock time for 2 simulations (0.002 m and 0.008 m in the grid independence study), ố – Orthogonality, ς – Skewness, AR – Aspect ratio.

Mesh Type: Hexahedral
Edge divisions: 80
Radial face divisions: 20
Number of elements: 665,600
Number of nodes: 700,560
Maximum skewness: 0.485
Minimum Orthogonality: 0.725
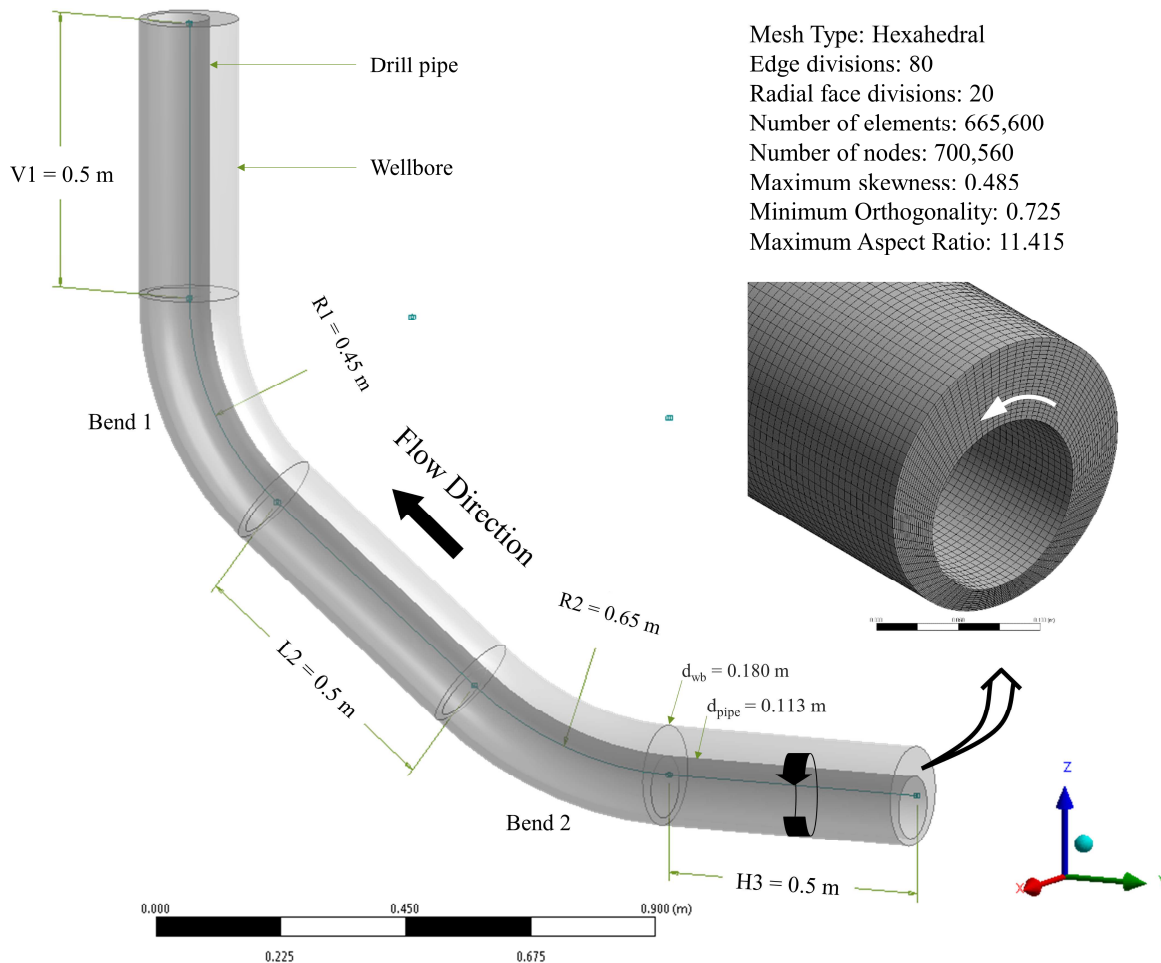Maximum Aspect Ratio: 11.415

Figure 1. Annular flow geometry

Figure 2 (our grid independence study) indicates that minor quantitative differences exist among the distinct mesh sizes applied: nevertheless, it is emphasized that all mesh resolutions (very coarse to very fine) used in all CFD simulations therein are in clear agreement, with similar particle deposition patterns at the bottom of the annulus.

Although no experimental data on flow through the geometry considered here with particle shape considerations exist, we apply similar principles of the CFD model development adopted here for validation purposes by using experimental data. We observe fairly good performance of our model with the data shown in Figure 3. It is observed that the cuttings concentration at the highest circulation rate was fairly difficult to predict; this could be attributed to the onset of turbulence thus creating complex particle-fluid interactions, experimental uncertainty which was not reported and missing data on the shape of particles. However, there is also a quantitative criterion for the minimum mesh control volume on which the volume averaged Eulerian-Eulerian continuum equations are valid for the solid phase.[41,42,43] Satisfying this condition for the range of volume fractions obtained in all mesh elements is cumbersome when realistic particle sizes and high eccentricities (similar to actual drilling campaigns) are considered: this is an inherent limitation of the continuum assumption employed for large particles, although convergence is always achieved. The application of Lagrangian–Eulerian models (specifically, Macroscopic Particle Models/MPM) tailored towards a more accurate description of large particles (bigger than a single mesh element in the lower annular section) can further reduce the prediction error, but at a higher computational cost.
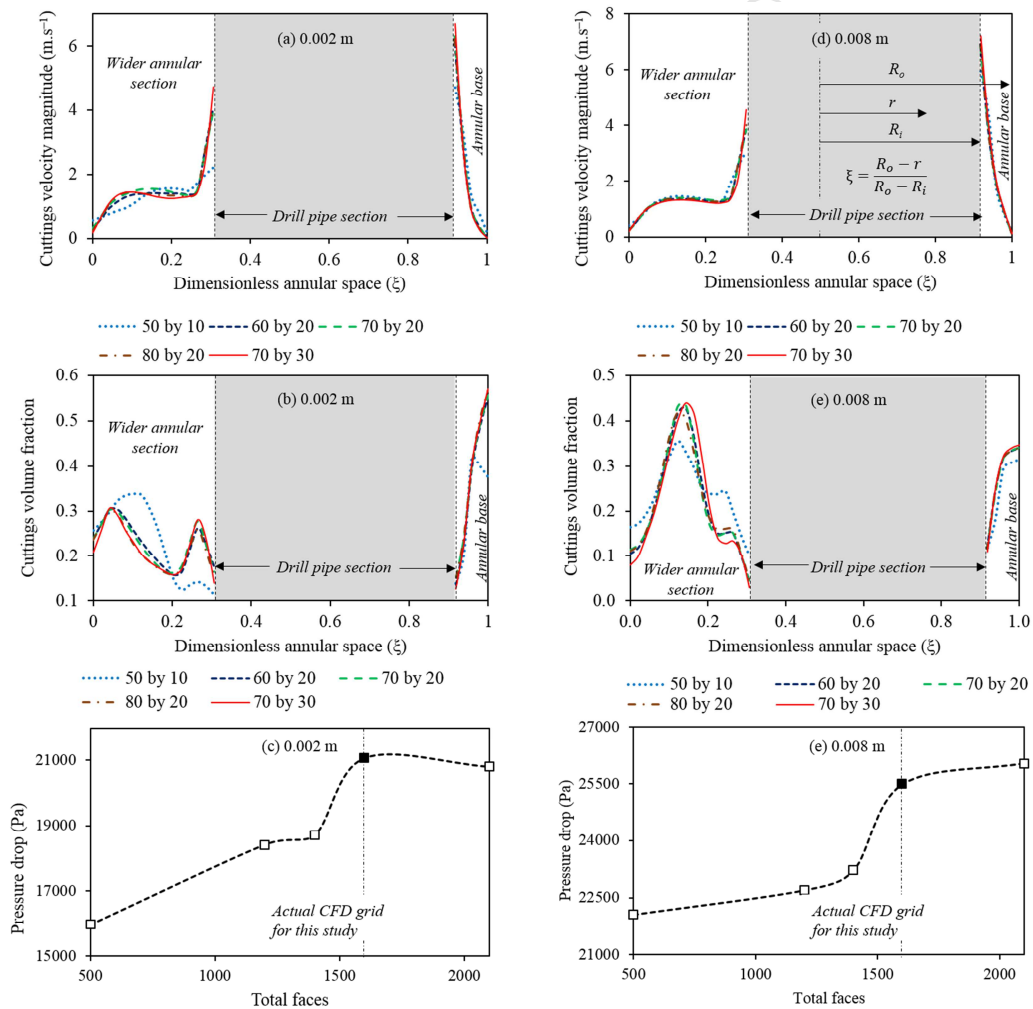
Figure 2. Grid independence study. Velocity and volume fraction profiles are obtained from the horizontal-to-inclined bend of the annulus at t = 5 seconds.

9
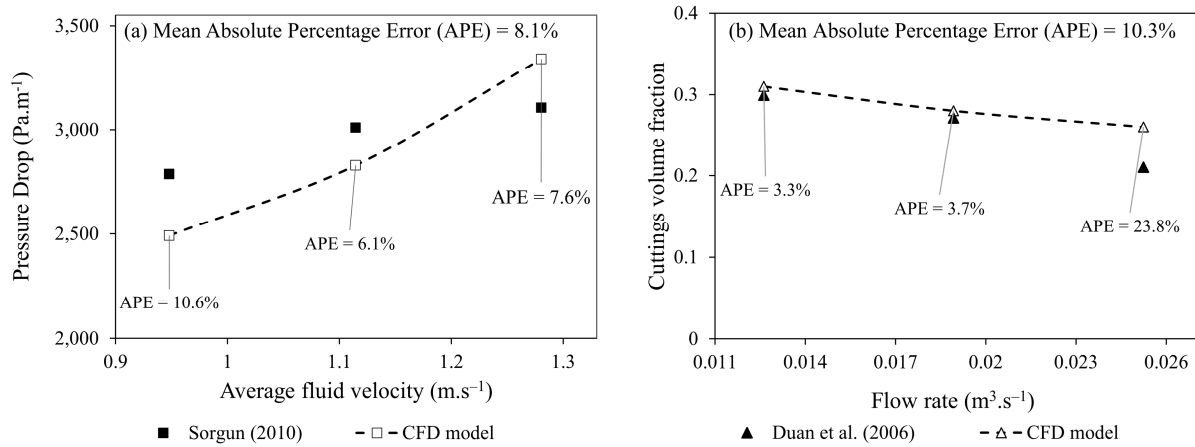
Figure 3. Validation of CFD model against experimental data

3. Results and Discussion

The computed time and volume averages of the particle velocities, volume fraction and overall pressure drop in the entire flow domain for a 5-second run time are presented and discussed. Results obtained using the two drilling fluids reveal considerable differences in rheological performance for the transport of cuttings of all sizes considered.

Figure 4. Skewed particle deposition in the annulus with a rotating drillpipe at 100 rpm for two different drilling fluid and comparison with Akshik et al[39]. A reduction in skewness is observed by using the second drilling fluid with superior rheological properties (b and d).

Before presenting the main results, it is important to demonstrate the concept of skewness in deposition patterns which is a vital finding of this work. As see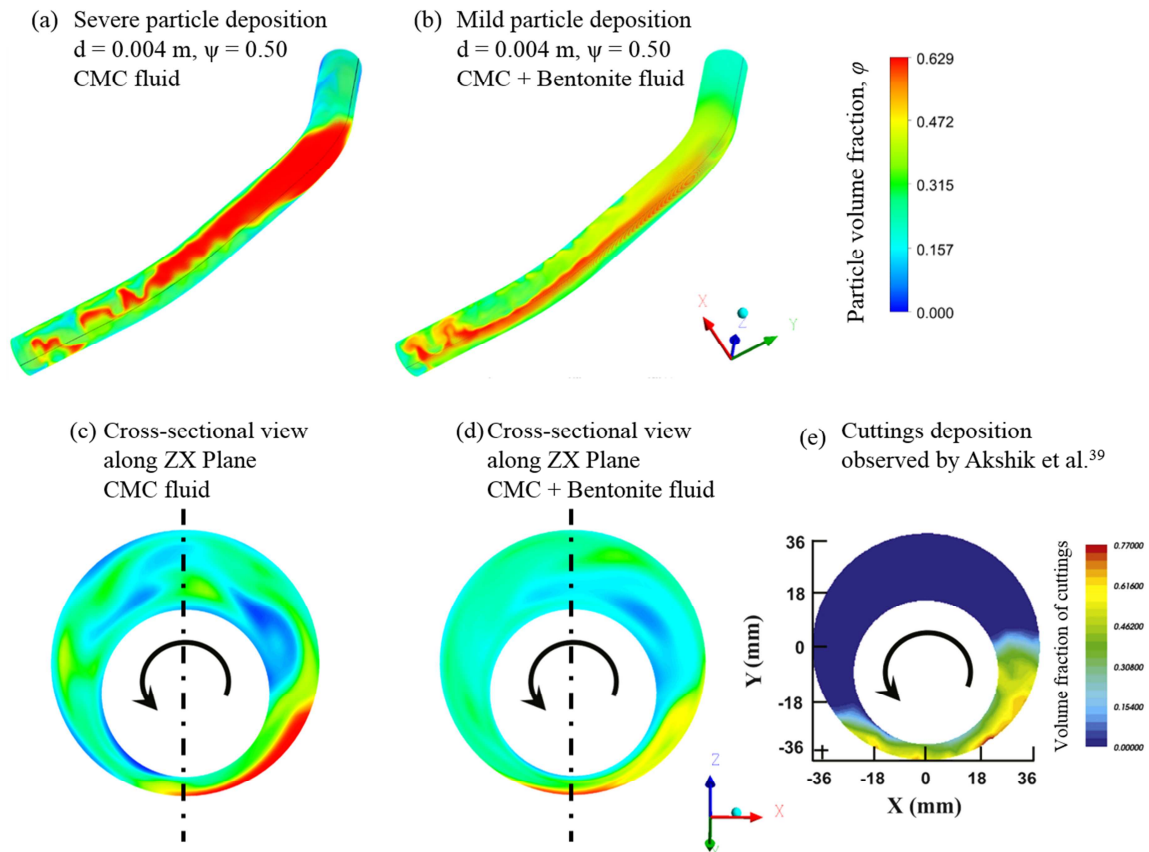n in Figure 4, cuttings deposition on either sides of the rotating drillpipe differ significantly. This depends on the drillpipe rotation and other factors which are subsequently explained. This phenomena was also observed by Akshik et al.[39] using the Discrete Element Method (DEM) coupled with CFD.

3.1 Cuttings velocity, volume fraction and pressure drop profiles using drill mud – 1

Figure 5 illustrates the behaviours of particles of different sphericities when transported with the 0.5 wt.% CMC drilling fluid. It is observed that non-spherical particles (of all diameters considered) remain longer in the bulk flow and travel faster than perfectly spherical particles before settling at the base of the annulus (Figures 5a and 5d). This finding agrees with experimental observations of Byron[28] and numerical investigations of Yilmaz[33]. The secondary motion (oscillatory and tumbling) exhibited by non-spherical particles when transported by a fluid tends to reduce the settling velocity compared to spherical particles.[10] This increased settling velocity of perfectly spherical particles in the partially inclined geometry considered here is the most probable reason for the increased deposition as shown in Figure 5d. The studies of Losenn[29] and Njobuenwu and Fairweather[30] further pointed out that non-spherical particles experience a higher dispersion effect compared to spherical particles due to the action of lift forces; this dispersion effect usually aids the transport process. Irregular particles generally have a higher drag coefficient than regular particles; Yow et al.[31] reported that this increased drag coefficient decreases the response time in the fluid, thus enabling better response to velocity fluctuations as shown in Figure. 5a. Thus, spherical particles whose primary motion is to roll towards or against the principal axial flow direction in a cuttings bed could in combination with their settling behaviour, pose greater resistance to flow compared to the frictional resistance of irregular particles (due to increased interparticle and particle-wall contact area).
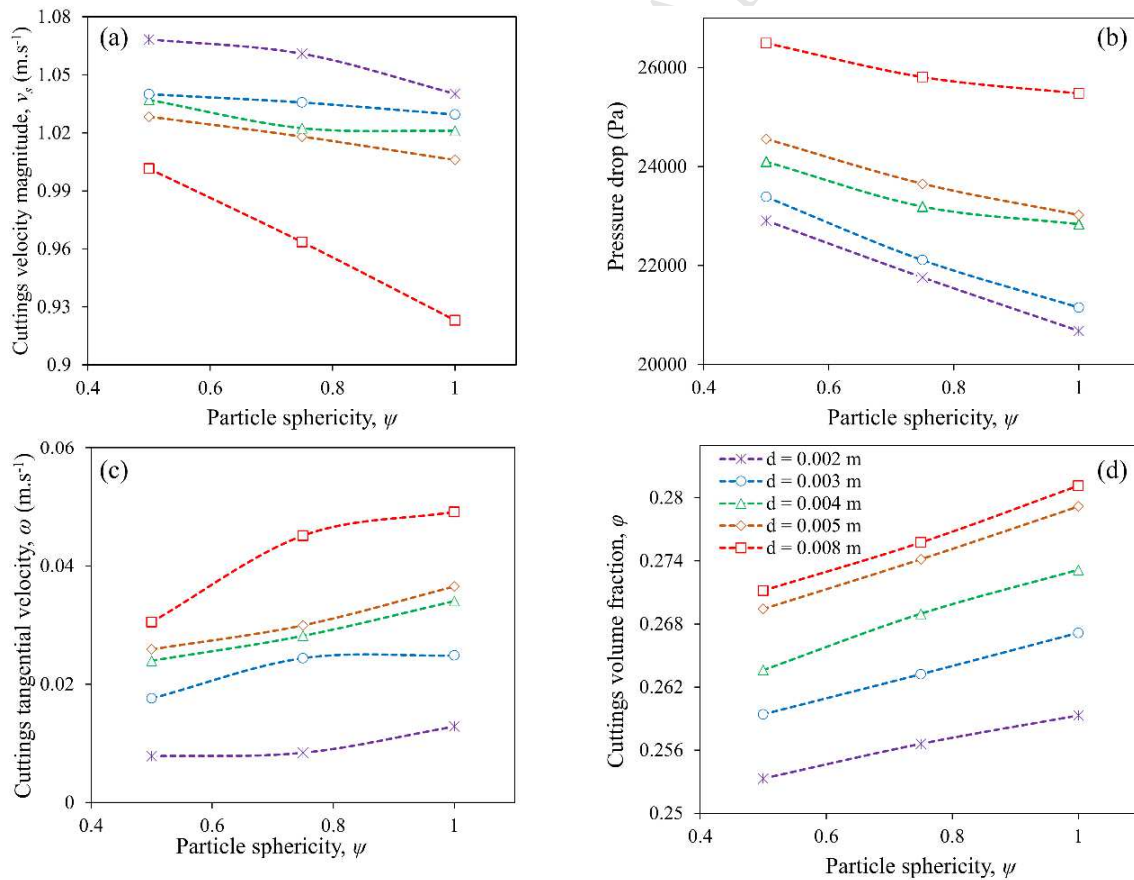

Figure 5. Profiles of volume-averaged and time-averaged cuttings velocity magnitude, tangential velocity, pressure drop and volume fraction for sphericities of 0.5, 0.75 and 1.0 respectively using drilling mud – 1.

It is also observed in Figure 5a that drill cuttings with 0.002 m diameter travel faster in the annulus than the larger cuttings (> 0.002 m) with higher inertia. However, a stronger tangential motion is noticed with the larger particles (Figure 5c). Also depicted in Figure 5c is the behaviour of different particle shapes with respect to their tangential velocities. It is observed that spherical particles will more readily respond to the tangential motion of the rotating drillpipe compared to non-spherical particles which exhibit a more chaotic flow behaviour. Particles with sphericity of 0.5 yield the lowest tangential velocity. It is important to differentiate the inherent oscillatory motion of non-spherical particles from their tangential motion due to drillpipe rotation. While this oscillatory motion is usually about the particles' axis, it may be independent of the principal axis of the rotating drillpipe. We infer that the combined effects of oscillatory and tangential motion yield the increased dispersion of the non-spherical particles in the flow domain earlier pointed out.

Anisotropic stress distribution produced by non-spherical particles, increased velocity due to secondary motion, higher particle-fluid interactions coupled with the increased drag and frictional forces are the most probable reasons for the increased pressure drop observed with the non-spherical particles compared to those of perfect sphericity (Figure 5b). As observed, these effects increase in magnitude with an increase in particle diameter and reduced sphericity. The impact of particle shape appears to be more significant on the transport velocity of the largest particles (0.008 m) relative to the smaller particles (Figure 5a). We further observe that for particles of ψ = 0.5, the assumption of absolute sphericity (ψ = 1) could yield a decrease of 11%, 10%, 6%, 7% and 4% in pressure drop for the 0.002 m, 0.003 m, 0.004 m, 0.005 m and 0.008 m particles respectively (Figure 5b). Similarly, approximately 5% decrease in cuttings volume fraction ensues between perfectly spherical particles and particles of 0.5 sphericity for all particle diameters (Figure 5d). These numerical differences provide some insight into the disparities that could arise when the results of CFD simulations with a perfectly spherical assumption for the cuttings are applied to the design of practical drilling operations, which usually involve cuttings of varying sphericities and a non-uniform size distribution.

3.2 Contour plots of volume fraction using drilling mud – 1

Increased particle deposition is generally observed at the inclined-to-vertical (upper bend) of the annulus compared to other regions. This deposition is also observed in the inclined section of the annulus with the 0.002 m particles displaying a more even deposition pattern (Figures 6a-c). The skewed deposition patterns of the larger particles (> 0.002 m) further explain the stronger impact of drillpipe rotation on the larger particles as seen in Figures 6d-o. This skewness is particularly noticed in the inclined and horizontal sections of the annulus and its effect increases with the particle diameter). The rotary drillpipe motion has been shown to sway particles in the direction of rotation[16]; thus yielding the skewed deposition observed with the larger particles (Figures 6d-o).

This phenomena is further reflected in the relatively uniform particle concentrations (Figures 6j-o) in the horizontal and inclined sections compared to the varying particle distribution (yellow patches) observed with the smaller particles (< 0.005 m) (Figures 6a-l). However, the impact of gravity as noticed in the vertical section (Figures 6j-o) is stronger because of the relatively heavier particles involved. Conversely, the vertical section (Figures 6a-l) is observed to be more uniform in particle distribution (and more densely concentrated), since lighter particles experience an apparent reduction in gravitational resistance in the carrier fluid.
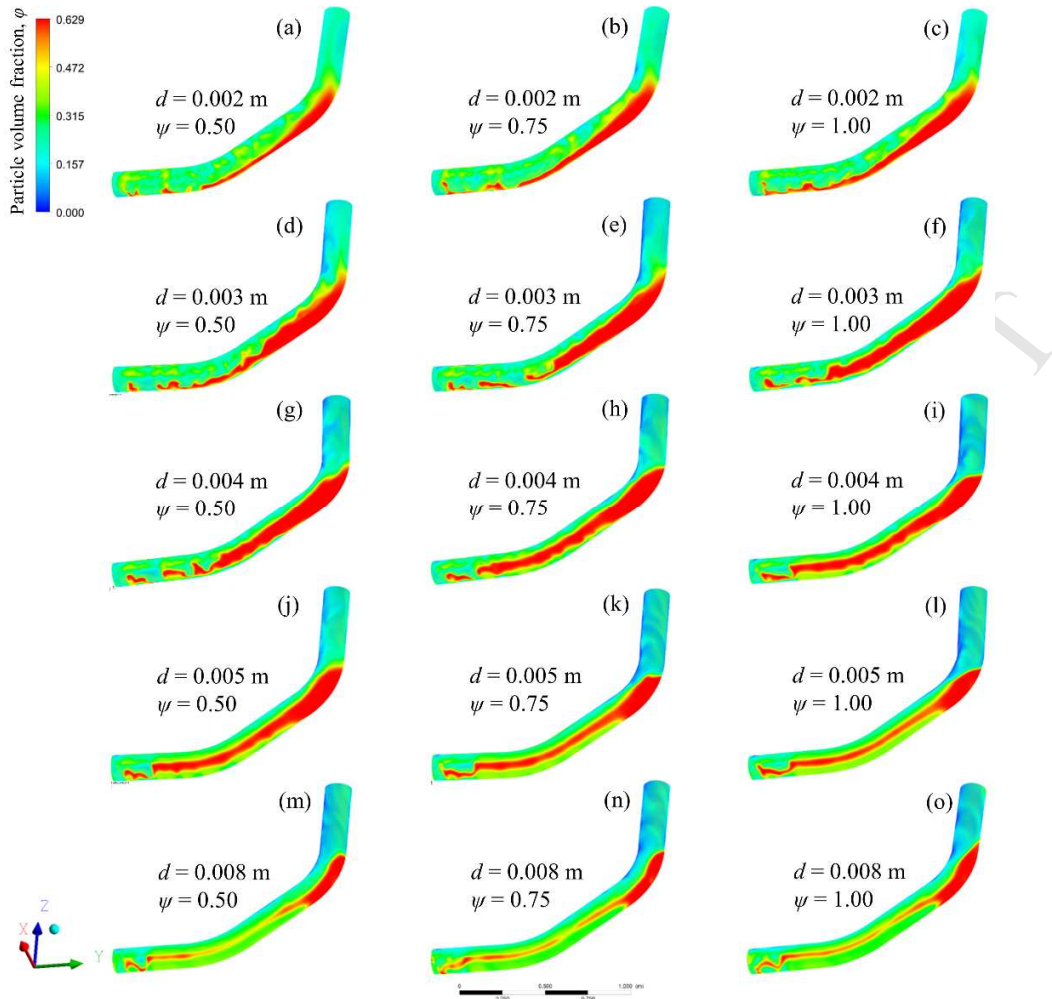
12

Figure 6. Contour plots (at 5 seconds) showing the impact of particle diameter and sphericity on the volume fraction in the annulus using drilling mud – 1.

3.3 Cuttings velocity, volume fraction and pressure drop profiles using drill mud – 2

Very similar flow property trends were observed with the first case (drill mud – 1). However, it can be seen that cuttings travel at a slightly higher velocity with the rheological improvement of the drill mud (Figures 5a and 7a). This viscosity improvement coupled with the increased transport velocity yield a corresponding higher pressure drop for all particle diameters (Figures 5b and 7b). Additionally, Figure 7c shows slightly reduced cuttings tangential velocities compared to Figure 5c (using the lower quality drilling mud). This implies that the improved drilling mud basically reduces the cuttings tangential motion by enhancing the transport of cuttings in the principal bulk flow direction. A major difference between the performances of both fluids is reflected in the cuttings volume fraction (particle concentration) profiles as shown in Figure 7d. Unlike the first drilling mud which showed a higher volume-averaged particle concentration for the 0.008 m particles compared the cuttings of smaller diameters, drilling mud – 2 reveals a rather different phenomena. Is it important to mention that the volume averaged cuttings concentration (Figure 7d) considers both the suspended and deposited cuttings in the averaging procedure throughout the flow domain; thus a more descriptive indication of transport phenomena may be obtained from the contour plots (Figure 8). Additionally, the actual mean volume fraction and its change with sphericity observed here is much lower than that observed with the first drilling mud. Compared to the 5% reduction earlier noticed with all particle diameters (Figure 5d), the change in volume fraction here is less than 0.7% for all particle diameters (Figure 7d).
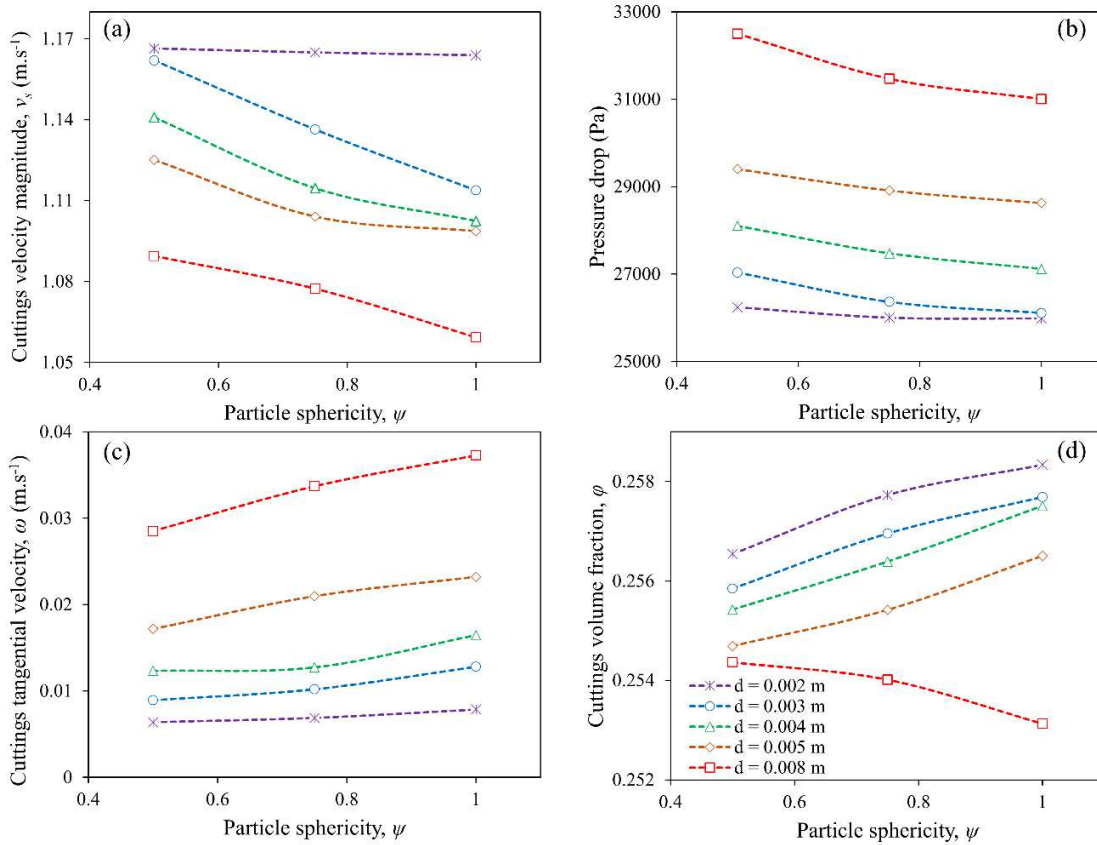
13

Figure 7. Profiles of volume-averaged and time-averaged of cuttings velocity magnitude, tangential velocity, pressure drop and volume fraction for sphericities of 0.5, 0.75 and 1.0 respectively using drilling mud – 2.

The reverse volume fraction profile observed with the 0.008 m particles (Figure 7d) indicates that frictional resistance of non-spherical particles plays a dominating role in the transport process compared to the (usually higher) settling velocities of spherical particles. However, the bulk velocity profile (Figure 7a) is retained for the 0.008 m particles. This phenomena is attributed to the reduced cross sectional area (due to increased deposition of the non-spherical particles) which yields an increased averaged velocity.[15] The slip velocity profile observed for the 0.008 m particles also further reflects the non-conformity observed in Figure 7d; this, we attribute to the alternating dominance of frictional and drag forces during transport. Considering the significant impact of cuttings diameter on the flow phenomena, it is worthwhile to investigate (in future work), the nature of particle deposition that ensues when a non-uniform size distribution of cuttings is applied.

3.4 Contour plots of volume fraction using drilling mud – 2

Figure 8(a-c) show a uniform distribution of the cuttings (0.002 m) around the annulus with only slight deposition at the base of the flow domain; improved transport (particularly with $\psi = 0.5$ and $\psi = 0.75$ – Figures 8j-k) is also noticed for the 0.005 m cuttings. This is due to the increased carrying capacity of the superior drilling mud. However, with 0.008 m particles, increased particle deposition occurs (Figures 8d-f). This deposition appears to be more significant compared to results obtained with the first drilling mud (Figures 6d-f); thus indicating that an increase in the mud viscosity does not always guarantee improved transport of drill cuttings. Cuttings deposition close to the drill bit is particularly increased (Figures 8m-o) compared to the first case (Figures 6m-o). An explanation of the observed phenomena could be derived from the increased resistance the highly viscous fluid poses to the rotary drillpipe motion; which induces a reduction in penetration rate (ROP) in industrial applications; CFD studies are hence paramount to the delicate rheological design of drilling muds in any practical operation.
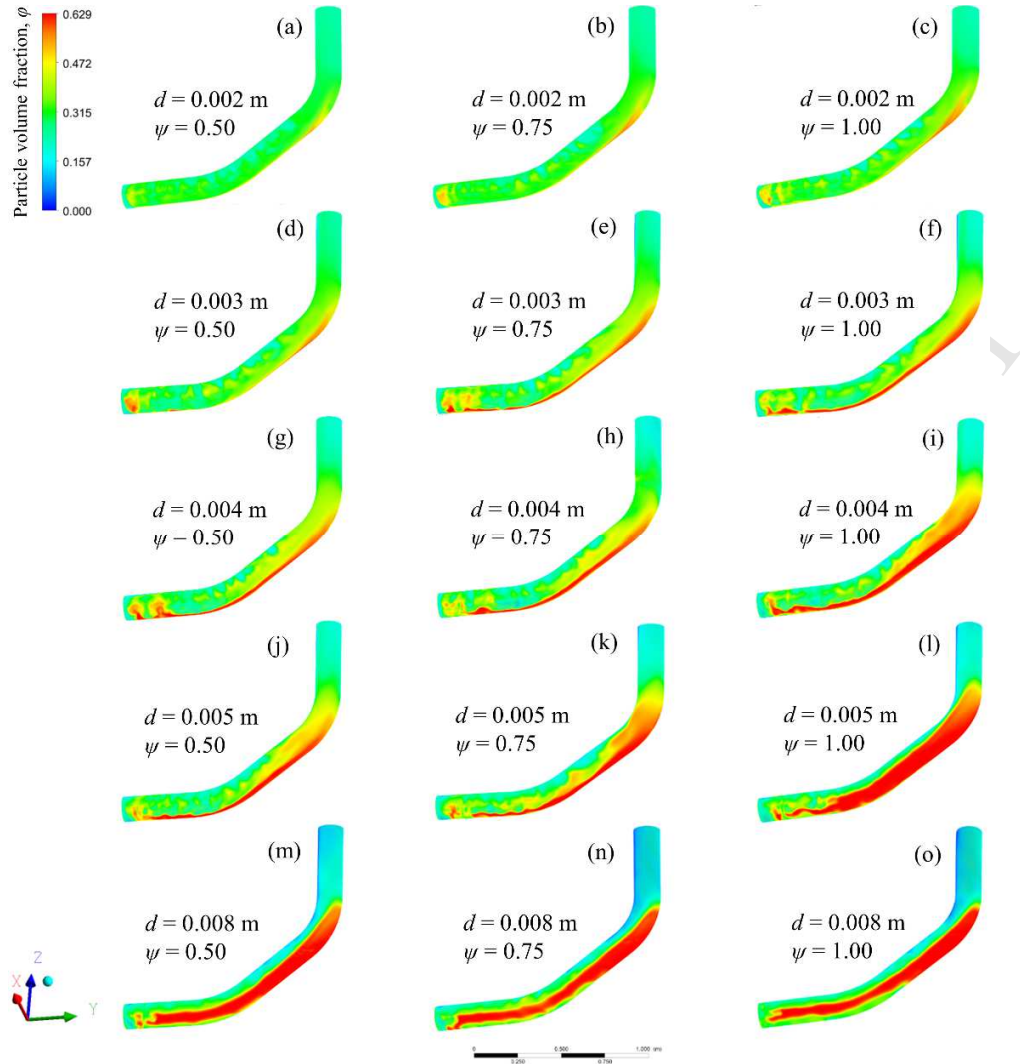
Figure 8. Contour plots (at 5 seconds) showing the impact of particle diameter and sphericity on the volume fraction in the annulus using drilling mud – 2.

We also observe that for particles of $\psi = 0.5$, the assumption of absolute sphericity ($\psi = 1$) yields a decrease of 1%, 3.5%, 3.5%, 4.4% and 5% in pressure drop for the 0.002 m, 0.003 m, 0.004 m, 0.005 m and 0.008 m particles respectively (Figure 7b).These are generally lower than the reductions observed with the first drilling mud; thus implying that the complexities of particle shape can be mitigated by a high quality drilling mud. The minor differences in volume fraction (Figure 7d) earlier explained also substantiate this deduction. Compared to Figure 6, we observe that the skewness in cuttings deposition is significantly decreased by using a superior drilling mud. These deposition patterns generally observed are not only determined by drillpipe rotation and gravitational forces, but also the eccentric geometry of the annulus. This narrower lower area of the annulus causes severe flow restrictions for the cuttings and hence accumulation.

It is also generally observed in Figures 6 and 8 that, three separate regions exist in the annulus considered: the region of intense cuttings deposition (red), regions of mild cuttings concentration (yellow), and regions with very low concentration of the cuttings (light green/blue). We liken these regions to the stationary bed, moving bed and heterogeneous suspension experimentally observed in the work of Doron and Barnea.[32]

15

3.5 Particle slip velocities and streamlines

The time and volume averaged slip velocities of the small and large particles of different sphericities are shown in Figure 9. It is illustrated that larger particles have a higher slip velocities compared to the smaller particles.
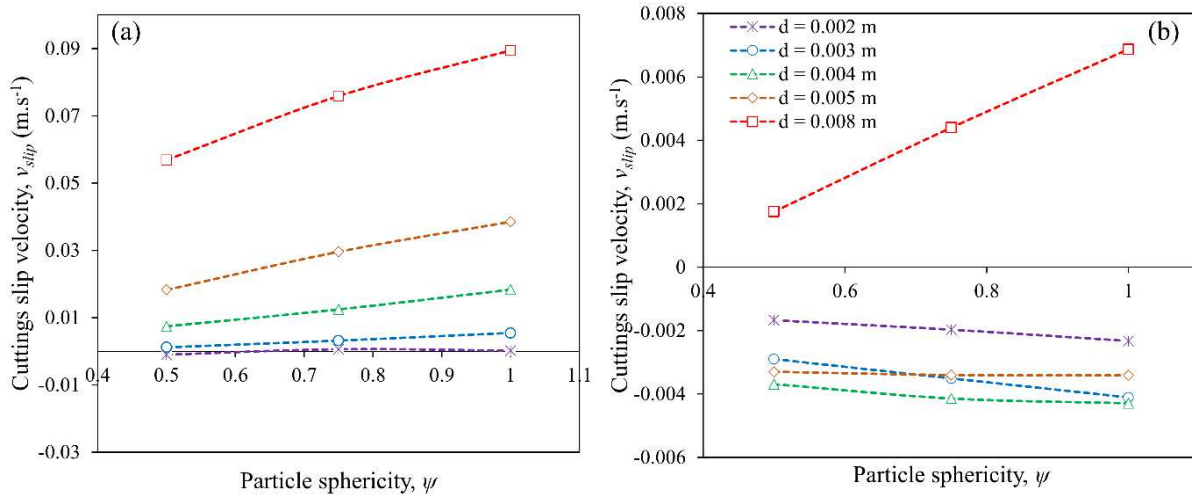
Figure 9. Cuttings slip velocities at different sphericities using drilling mud 1 (a) and drilling mud 2 (b).
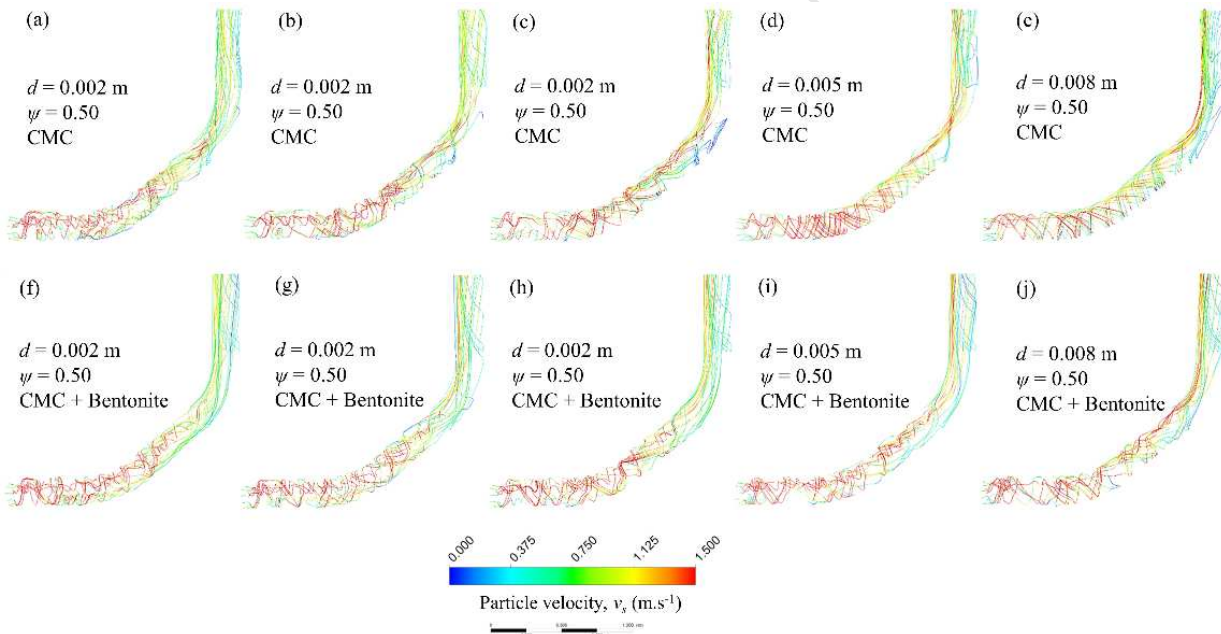
Figure 10. Streamlines of particle velocity (at 5 seconds) for all diameters and a sphericity of 0.5 using drilling – mud 1 and 2.

Epelle and Gerogiorgis[16] attributed this effect to the higher spreading tendencies of smaller particles and the ability of smaller-sized particles to readily follow/respond to the motion of the fluid. The relatively smooth and spherical particles would have less contact time with the fluid than non-spherical particles during flow interactions; thus yielding higher slip velocities. Conversely, the secondary motion exhibited by non-spherical particles enables increased particle-fluid interaction; hence the lower slip velocities encountered (Figures 9a and b). With the second drilling mud (of higher viscosity), the slip velocities of the larger particles observed are much lower (by an order of magnitude) compared to the lower viscosity mud; thus demonstrating its superior carrying capacity.

The particle streamlines shown in Figure 10 (a-j) indicate that the impact of drill pipe rotation on particle motion in the vertical section of the annulus is much lower compared to the inclined and horizontal sections respectively. This effect was noticed for all particle sphericities considered. Furthermore, this reduced impact of drillpipe rotation due to the transition in the annular geometry coupled with the eccentric configuration of flow, are the major reasons for increased particle deposition noticed around the bend (inclined-to-vertical) compared to other areas in the annulus. It is also observed (Figure 10) that the rotary motion of cuttings induced by the drillpipe is stronger in the in the CMC fluid (Figures 10a-c) compared to the streamlines of cuttings velocity, when the superior drilling mud is used (Figures 10f-j). This further demonstrates the increased axial bulk transport of cuttings the superior drilling mud provides.

4. Conclusions

It is evident from this study that flow characteristics present in practical applications are different but however share some similarities with a single-particle flow in a fluid. The presence of other interacting particles and bounding walls (stationary and rotating) in the flow domain are the main sources of increased complexity. By implementing the Eulerian-Eulerian model, we have been able to determine the flow peculiarities non-spherical cuttings add to the transport phenomena in an annular flow geometry. This was specifically achieved by incorporating the particle sphericity into the interphase exchange coefficient of the Syamlal-O'Brien drag model. The following conclusions can be drawn from the observations made in this study:

- Compared to other regions in the flow domain, the inclined-to-vertical (upper) bend is the most susceptible location to particle deposition. The combined effects of annular eccentricity and gravitational resistance are the main reasons for this observation.
- Non-spherical particles generally experience increased dispersion and travel faster than perfectly spherical particles in the annulus. We attribute this observation to the secondary motion usually experienced by non-spherical particles.
- As far as the cuttings transport velocity is concerned, the impact of particle sphericity is more significant with the larger (0.008 m) particles compared to the smaller-sized particles (0.002 m - 0.005 m).
- Drillpipe rotation has a more pronounced impact on larger particles, especially in the horizontal and inclined regions of the annulus. An increased skewness in the deposition pattern occurs with larger particles compared to those of a smaller size.
- Drill cuttings assume a near-rectilinear motion in the vertical annular sections compared to the rather chaotic motion observed in other sections of the annulus.
- With the application of drilling mud – 1, the assumption of a perfectly spherical particle geometry (ψ = 1.0 in place of ψ = 0.5) could lead to a decrease of 11%, 10%, 6%, 7% and 4% in the actual pressure drop for 0.002 m, 0.003 m, 0.004 m, 0.005 m and 0.008 m particles respectively. These differences are much lower when using the second drilling fluid of superior rheology. Reliable predictions of cuttings deposition, re-suspension, dispersion and carrier fluid pumping requirements thus depend on the particle shape especially when the project's economics constrain the choice of drilling mud.
- Sectional analysis of cuttings deposition along several planes in the annulus provided better variability in cuttings concentration as a function of particle sphericity compared to the volume average analysis.
- Viscosity improvement (by the addition of 4 wt.% Bentonite) to the basic drilling mud (0.5 wt.% CMC) increases the cuttings transport efficiency particularly with smaller-sized particles. This increase is not always guaranteed when larger particles are transported due to increased particle deposition (beyond that noticed with a less viscous mud). Thus, the application of optimisation techniques for CFD/fluid rheological design particularly considering the complex particle deposition tendencies is an area that deserves more attention.

Experimental investigations of drill cuttings transport phenomena that consider the effect of particle shape are extremely scarce; this influenced our relatively straightforward implementation of the sphericity coefficient. Incorporating the effects of the particle aspect ratio, incidence angle and orientation in the drag and lift forces is a more sophisticated modification of the Eulerian-Eulerian multiphase flow model and constitutes an area where

future efforts should be targeted; such efforts would be motivated by the availability of experimental data. It will be also worthwhile to evaluate the improvement in experimental data prediction by including these extra parameters (asides the sphericity and volume equivalent diameter used in this work). Due to the model limitations discussed, we aim to explore adaptive mesh procedures which refine cell sizes based on the local instantaneous solid volume fraction in the entire computational domain. With this technique, a limit can be enforced on the spatial grid sizes, towards ensuring the validity of the Eulerian continuum assumptions on the solid phase. The application of the sphericity coefficient in the Eulerian multiphase model in this paper has successfully shown that flow dynamics of perfectly spherical particles differ considerably from those of non-spherical particles with an equivalent volume diameter and density; the quantification of this disparity is of definite industrial importance.

Nomenclature and Acronyms

Latin letters

A,B,c,d	Coefficients of the Syamlal-O'Brien drag model (-)	I_{2D}	Second variant of the deviatoric stress (-)
c_t	Cuttings concentration threshold	$\bar{\bar{I}}$	Unit tensor (-)
A_c	Particle surface area (m²)	K_{sl}	Interphase momentum exchange coefficient (-)
A_s	Surface area of volume equivalent sphere (m²)	$\acute{K}_{sl}$	Modified interphase exchange coefficient (-)
C_D	Drag coefficient (-)	K	Consistency index (Pa.s^n)
CMC	Carboxymethyl cellulose solution	$\dot{m}_{sl}$	Mass transfer from phase s to phase l (kg.s⁻¹)
d_s	Volume equivalent particle diameter (m)	$\dot{m}_{ls}$	Mass transfer from phase l to phase s (kg.s⁻¹)
e	Eccentricity (-)	n	Flow behaviour index (-)
e_{ss}	Coefficient of restitution (-)	p	Pressure (Pa)
F_r,n,p	Constants in the frictional pressure equation	p_s	Solids pressure (Pa)
$\vec{F}_{lift,s}$	Lift force (N)	ROP	Rate of Penetration (ft.hr⁻¹)
$\vec{F}_s$	External body force (N)	Re_s	Particle Reynolds number (-)
$\vec{F}_{wl,s}$	Wall lubrication force (N)	S_q	Source term (-)
$\vec{F}_{d,s}$	Turbulent dispersion force (N)	τ_0	Yield Stress (N.m⁻²)
$\vec{F}_{lift,s}$	Lift force (N)	u_m	Mean flow velocity (m.s⁻¹)
$\vec{F}_{vm,s}$	Virtual mass force (N)	$\vec{v}_{sl}$	Interphase velocity (m.s⁻¹)
$\vec{F}_{td,s}$	Turbulent dispersion force (N)	$\vec{v}_s$	Solid phase velocity (m.s⁻¹)
g	Gravitational acceleration (m.s⁻²)	$\vec{v}_l$	Liquid phase velocity (m.s⁻¹)
$g_{0,ss}$	Compressibility transition function (-)	$v_{r,s}$	Terminal velocity (m.s⁻¹)
		v_{slip}	Cuttings slip velocity (m.s⁻¹)

Greek letters

α_s	Solid phase volume fraction (-)
$\alpha_{s,max}$	Solid volume fraction at maximum packing (-)
$\alpha_{s,min}$	Solid volume fraction after which friction occurs (-)
α_l	Liquid phase volume fraction (-)
$\mu_{s,kin}$	Kinetic viscosity (Pa.s)
$\mu_{s,fr}$	Frictional viscosity (Pa.s)
λ_s	Bulk viscosity (Pa.s)
λ_q	Primary phase bulk viscosity (Pa.s)
μ_l	Fluid viscosity (Pa.s)
μ_q	Primary phase viscosity (Pa.s)
Θ_s	Granular temperature (K)
ρ_s	Solid phase density (kg.m⁻³)
$\rho_{r,s}$	Phase reference density (kg.m⁻³)
ρ_q	Primary phase density (kg.m⁻³)

18

ρ_f	Fluid density (kg.m^{-3})
$\hat{\rho}_q$	Effective phase density (kg.m^{-3})
β	Hole inclination angle (degrees)
ψ	Particle sphericity (-)
ζ	Dimensionless annular space (-)
φ	Cuttings bed porosity (%)
δ	Offset distance (m)
ϕ	Angle of internal friction (degrees)
ϕ_{ls}	Energy exchange between fluid and solid phases (kg.m^{-1}s^{-3}))
η	Drag modification factor
α_l	Fluid phase volume fraction (-)
α_s	Solid phase volume fraction (-)
τ	Shear stress (N.m^{-2})
$\bar{\bar{\tau}}_s$	Solid phase stress tensor (-)
γ	Shear rate (s^{-1})
$\gamma_{\Theta s}$	Collisional dissipation of energy (kg.m^{-1}s^{-3})

Literature References

1. Sobieski, W., 2009. Switch function and sphericity coefficient in the Gidaspow drag model for modeling solid-fluid systems. *Drying Technol.* 27(2), 267-280.

2. Comer, J.K. and Kleinstreuer, C., 1995. A numerical investigation of laminar flow past nonspherical solids and droplets. *Transactions-ASME J. Fluids Eng.* 117, 170-175.

3. Epelle, E.I. and Gerogiorgis, D.I., 2017a. A multiparametric CFD analysis of multiphase annular flows for oil and gas drilling applications. *Comput. Chem. Eng.*106, 645-661.

4. Ofei, T., Irawan, S., & Pao, W., 2014. CFD method for predicting annular pressure losses and cuttings concentration in eccentric horizontal wells. *J. Pet. Eng.*

5. Rooki, R., Ardejani, F.D., Moradzadeh, A. and Norouzi, M., 2015. CFD Simulation of Rheological Model Effect on Cuttings Transport. *J. Dispersion Sci. Technol.* 36(3), 402-410.

6. Heydari, O., Sahraei, E., & Skalle, P., 2017. Investigating the impact of drillpipe's rotation and eccentricity on cuttings transport phenomenon in various horizontal annuluses using computational fluid dynamics (CFD). *J. Pet. Sci. Eng.* 156, 801-813.

7. Ding, E.J. and Aidun, C.K., 2000. The dynamics and scaling law for particles suspended in shear flow with inertia. *J. Fluid Mech.* 423, 317-344.

8. Karnis, A., Goldsmith, H.L. and Mason, S.G., 1963. Axial migration of particles in Poiseuille flow. *Nature*, 200(4902), 159-160.

9. Karnis, A., Goldsmith, H.L. and Mason, S.G., 1966. The flow of suspensions through tubes: V. Inertial effects. *The Can .J. Chem. Eng.* 44(4), 181-193.

10. Mandø, M., Yin, C., Sørensen, H. and Rosendahl, L., 2007. On the modelling of motion of non-spherical particles in two-phase flow. In *6th Int. Conference Multiphase Flow. ICMF*, 9-13.

11. Qi, D. and Luo, L.S., 2003. Rotational and orientational behaviour of three-dimensional spheroidal particles in Couette flows. *J. Fluid Mech.* 477, 201-213.

12. Hua, L., Zhao, H., Li, J., Wang, J. and Zhu, Q., 2015. Eulerian–Eulerian simulation of irregular particles in dense gas–solid fluidized beds. *Powder Technol.* 284, 299-311.

13. Sobieski, W., 2010. Drag Coefficient in Solid–Fluid System Modeling with the Eulerian Multiphase Model. *Drying Technol.* 29(1), 111-125.

14. Reuge, N., Cadoret, L., Coufort-Saudejaud, C., Pannala, S., Syamlal, M. and Caussat, B., 2008. Multifluid Eulerian modeling of dense gas–solids fluidized bed hydrodynamics: influence of the dissipation parameters. *Chem. Eng. Sci.* 63(22), 5540-5551.

15. Akhshik, S., Behzad, M. and Rajabi, M., 2016. CFD-DEM simulation of the hole cleaning process in a

deviated well drilling: The effects of particle shape. *Particuology. 25*, 72-82.

16. Epelle, E.I. and Gerogiorgis, D.I., 2017b. Transient and Steady State Analysis of Drill Cuttings Transport Phenomena under Turbulent Conditions. *Chem. Eng. Res. Des.,* in press.

17. Fluent, A. (2017). 18.0 ANSYS Fluent theory guide 18.0. *Ansys Inc*, U.S.A.

18. Chhabra, R.P., Agarwal, L. and Sinha, N.K., 1999. Drag on non-spherical particles: an evaluation of available methods. *Powder Technol.* 101(3), 288-295.

19. Syamlal, M. and O'Brien, T.J., 1987. The derivation of a drag coefficient formula from velocity-voidage correlations. *Technical Note, US Department of energy, Office of Fossil Energy, NETL, Morgantown, WV.*

20. Dalla Valle, J.M., 1943. Micromeritics the Technology of Fine Particles. Pitman Publishing Corporation. New York.

21. Gidaspow, D., 1994. Multiphase flow and fluidization: continuum and kinetic theory descriptions. Academic press. NewYork

22. Syamlal, M., Rogers, W. and O'Brien, T.J., 1993. MFIX documentation: Theory guide. *National Energy Technology Laboratory, Department of Energy, Technical Note DOE/METC-95/1013 and NTIS/DE95000031.*

23. Lun, C., Savage, S., & Jeffrey, D., 1984. Kinetic theories for granular flow: inelastic particles in Couette flow and slightly inelastic particles in a general flowfield. *J. Fluid Mech.* 140, 223-256.

24. Schaeffer, D., 1987. Instability in the evolution equations describing incompressible granular flow. *J. Diff. Eqns.* 66(1), 19-50.

25. Johnson, P. C., & Jackson, R., 1987. Frictional–collisional constitutive relations for granular materials, with application to plane shearing. *J. Fluid Mech.* 176, 67-93.

26. Abu-Jdayil, B. and Ghannam, M., 2014. The modification of rheological properties of sodium bentonite-water dispersions with low viscosity CMC polymer effect. *Energy Sources, Part A: Recovery, Utilization, and Environmental Effects.* 36(10), 1037-1048.

27. Clift, R., Grace, J.R. and Weber, M.E., 2005. Bubbles, drops, and particles. Courier Corporation. Massachusetts.

28. Byron, M.L., 2015. The rotation and translation of non-spherical particles in homogeneous isotropic turbulence. PhD Thesis, University of California, Berkeley, USA.

29. Losenno, C.G.R., 2004. An investigation of irregular particles in free-fall. PhD thesis, University of Edinburgh.

30. Njobuenwu, D.O. and Fairweather, M., 2014. Effect of shape on inertial particle dynamics in a channel flow. *Flow, turbulence and combustion.* 92(1-2), 83-101.

31. Yow, H.N., Pitt, M.J. and Salman, A.D., 2005. Drag correlations for particles of regular shape. *Adv. Powder Technol.* 16(4), 363-372.

32. Doron, P., and Barnea, D. (1993). A three-layer model for solid-liquid flow in horizontal pipes. *Intl. J. Multiphase Flow*, 19(6), 1029–1043.

33. Yilmaz, D., 2012. Discrete Phase Simulations of Drilled Cuttings Transport Process in Highly Deviated Wells. Louisiana State University, USA, Master dissertation.

34. Duan, M., Miska, S.Z., Yu, M., Takach, N.E., Ahmed, R.M., Zettner, C.M., 2006. Transport of small cuttings in extended reach drilling. In: International Oil & Gas Conference and Exhibition in China. Society of Petroleum Engineers.

35. Al-Kayiem, H.H., Zaki, N.M., Asyraf, M.Z., Elfeel, M.E., 2010. Simulation of the cuttings cleaning during the drilling operation. Am. J. Appl. Sci. 7 (6), 800–806

36. Sorgun, M., 2010. Modeling of Newtonian Fluids and Cuttings Transport Analysis in High Inclination Wellbores with Pipe Rotation. Middle East Technical University, Turkey, Doctoral dissertation.

37. Mohammadzadeh, K., Hashemabadi, S.H. and Akbari, S., 2016. CFD simulation of viscosity modifier effect on cutting transport by oil based drilling fluid in wellbore. J. Nat. Gas Sci. Eng., 29, 355-364.

38. Vollmari, K., Jasevičius, R. and Kruggel-Emden, H., 2016. Experimental and numerical study of fluidization and pressure drop of spherical and non-spherical particles in a model scale fluidized bed. *Powder Technology*, 291, 506-521.

39. Akhshik, S., Behzad, M. and Rajabi, M., 2015. CFD–DEM approach to investigate the effect of drill pipe rotation on cuttings transport behavior. *J. Pet. Sci. Eng.* 127, 229-244.

40. Celigueta, M.A., Deshpande, K.M., Latorre, S. and Oñate, E., 2016. A FEM-DEM technique for studying the motion of particles in non-Newtonian fluids. Application to the transport of drill cuttings in wellbores. *Comput. Part. Mech.* 3(2), 263-276.

41. Clemiņš, A., 1988. Representation of two-phase flows by volume averaging. *Int. J. Multiphase Flow*, 14(1), 81-90.

42. Fan, L.S. and Zhu, C., 2005. Principles of gas-solid flows. Cambridge University Press.

43. Gómez, L.C. and Milioli, F.E., 2005. Numerical simulation of fluid flow in CFB risers: A turbulence analysis approach. *J. Braz. Soc. Mech. Sci. Eng.* 27(2), pp.141-149.